Superponderomotive regime of tunneling ionization

D. F. Gordon,* J. P. Palastro, and B. Hafizi
Beam Physics Branch, Plasma Physics Division, U.S. Naval Research Laboratory, Washington, DC 20375, USA
(Received 12 November 2015; published 6 March 2017)

Ultrarelativistic photoelectron spectra exhibit unexpected characteristics in a paraxial laser focus. The photoelectron energy scales superponderomotively, and the usual parabolic momentum distribution is distorted into a variety of intricate patterns, depending on the location of the ion. These patterns include discrete contours, which in some cases can be easily identified with a particular subcycle burst of ionization current. An analytical formula for the maximum photoelectron energy in a paraxial radiation field is given, and high-resolution momentum distributions with narrowly peaked features are presented. These narrowly peaked features suggest application to electron injection into plasma-based accelerators.

DOI: 10.1103/PhysRevA.95.033403

I. INTRODUCTION

As laser technology continues to advance, new regimes of laser-matter interaction appear. Serious efforts are currently under way to build multipetawatt laser facilities capable of delivering a focused irradiance of the order of 10^{23} W/cm^2. Such facilities open up new experimental possibilities in high-field physics (see, e.g., Ref. [1]). Relativistic tunneling ionization is a fundamental process that automatically accompanies any such experiment where the target composition includes atoms heavier than boron [2]. In this paper, a regime of tunneling ionization, characterized by superponderomotive energy scaling and accessible to multipetawatt lasers, is reported. Apart from its significance as a fundamental physical process, tunneling ionization of electrons in superstrong fields has applications in plasma-based accelerators [3–6].

The photoelectron distribution due to relativistic tunneling ionization is most often analyzed in the plane-wave approximation [7–10]. Finite-spot-size effects are generally thought to lead to a preference for photoelectron energies commensurate with the ponderomotive potential [3,4]. Full-scale three-dimensional *ab initio* simulations of relativistic photoionization are just now becoming possible [10], but even this state of the art does not permit determination of the wave function far enough from the interaction region to directly compute observable photoelectron distributions. On the other hand, the two-step model [11] can be employed to estimate photoelectron distributions far from the interaction region. This paper applies the two-step model to the case of tunneling ionization in a paraxial radiation focus, where the free electron dynamics are ultrarelativistic [12]. Under these conditions, the photoelectron distribution is qualitatively different from what is obtained under either plane-wave illumination or weakly relativistic paraxial illumination.

In tunneling ionization, the probability current near the barrier depends only on the instantaneous field [13,14] and is, therefore, strongly localized in phase. In an extreme field, it becomes possible for free electrons to remain localized in phase until they leave the confocal region. Such an electron is exposed to only a few radiation cycles before the field is geometrically attenuated and may be said to be in phase resonance with the electromagnetic wave (cf. Landau resonance [15]). This cannot happen in a plane wave, where there is no geometric attenuation. Important consequences of phase resonance include superponderomotive energy scaling and nonparabolic momentum-space contours. The laser power needed to readily observe these effects falls in the multipetawatt range.

The existing literature dealing with finite-spot-size effects in tunneling ionization includes Refs. [3,4], and [16–19], among others. The analysis, calculations, and experiments considered in Refs. [3] and [4] are in the ponderomotive regime and so do not address phase resonance. References [16] and [17] discuss phase resonance but lack analytical treatment and discussion of scaling with irradiance. References [16] and [17] utilize a classical model for the bound states, whereas the two-step model used here employs a quantum mechanical ionization rate [9] and includes radiation reaction [12] during the classical motion. The numerical approach [12] produces a highly resolved S matrix and momentum distributions which are, in principle, observable quantities that can be correlated with subcycle bursts of ionization current and may be useful for particle acceleration applications.

II. SUPERPONDEROMOTIVE PHOTOELECTRONS

Quantum mechanically, there is a finite probability of obtaining any photoelectron energy. In contrast, the quasiclassical two-step model produces a bounded photoelectron energy spectrum. The maximum energy is meaningful if the characteristic energy spread in the quasiclassical distribution is similar to the quantum mechanical energy spread, for then the probability of obtaining energies beyond the maximum is exponentially small. We verified that this is the case by comparing the two-step model with the Coulomb-corrected strong-field approximation in Ref. [9], in the appropriate limit.

The scaling of the maximum photoelectron energy with the radiation amplitude is shown in Fig. 1, with the radiation amplitude given in terms of the peak-normalized vector potential, $a_0 = eA_0/mc^2$. The parameter a_0 characterizes the importance of relativistic effects, i.e., when $a_0 \lesssim 1$ the free electron dynamics are weakly relativistic, while when $a_0 \gg 1$ they are ultrarelativistic. Each value of a_0 is paired with a particular ionization potential, $U_{\rm ion}$, shown on the upper horizontal axis. The $U_{\rm ion}$ values are

*daniel.gordon@nrl.navy.mil

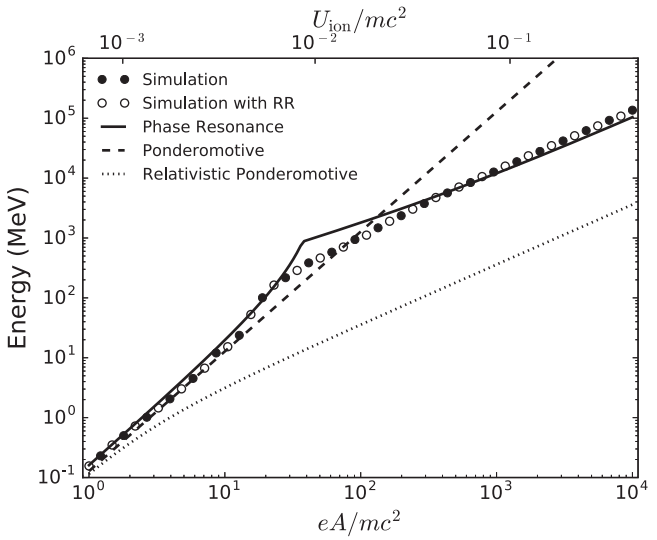

FIG. 1. Maximum energy in the photoelectron spectrum for an 0.8-μm-wavelength, 30-fs pulse, focused on a 5-μm spot, for a range of radiation amplitudes and matching ionization potentials. Pulse metrics are referenced to $1/e$ of the field.

chosen so that the corresponding a_0 is twice the threshold value for tunneling ionization. The plot shows simulation results, along with three theoretical curves for comparison (see derivation below).

Figure 1 illustrates several important points. First, two regimes of photoelectron generation are clearly suggested, one for $a_0 \lesssim 10$ and one for $a_0 \gtrsim 100$. The simulation results for $a_0 \leqslant 10$ are well matched by the theoretical curves labeled "ponderomotive" and "phase resonance." The ponderomotive model is just the prediction from Refs. [3] and [4], $u_0 = 1 + a_0^2/4$, where u_0 is the time component of the four-velocity. The phase resonance model is derived below. Results for $a_0 \gtrsim 100$ are well matched only by the phase resonance model. The relativistic ponderomotive curve, defined by $u_0 = \sqrt{1 + a_0^2/2}$, is wrong everywhere (this model applies in the quasistatic limit of laser-plasma interactions [20]). In the transition region, $10 \lesssim a_0 \lesssim 100$, quantitative accuracy is missing from all the models, but the correct qualitative behavior is capture by the phase resonance model. The compelling feature in Fig. 1 is the superponderomotive scaling of the energy with a_0, especially for $10 < a_0 < 30$. This scaling should be contrasted with that of the mass-corrected ponderomotive potential, which underestimates the energy by two orders of magnitude at the point where phase resonance sets in.

The simulation points in Fig. 1 alternate between runs that include and runs that do not include a classical radiation reaction. Clearly, the radiation reaction is found to have a minor effect on the maximum photoelectron energy. There is, however, an effect on the detailed momentum distribution, which becomes noticeable for $a_0 > 10^3$ (not shown). It should be noted that the radiation reaction model used here only affects the motion in the classical region and that quantum electrodynamics effects such as pair production are not accounted for (the highest field used is about 3% of the Schwinger limit). Ion motion is also neglected.

III. PHASE RESONANCE MODEL

The phase resonance model is based on the expectation that when an inner-shell electron is tunnel-ionized, it is accelerated abruptly to the speed of light. In this limit, the motion is nearly parallel to the wave vector of the radiation, and the phase of the particle in the radiation field can be regarded as constant. The primary constraint is that the interaction is limited to regions where the irradiance is high and the phase velocity is close to c. This corresponds to the two regions just outside the confocal region. That is, far from the confocal region the irradiance is too low, but inside the confocal region the phase velocity is too high.

Let the four-dimensional coordinate and velocity of an electron be denoted x and u, respectively. Consider the lowest order, linearly polarized, Hermite-Gaussian laser mode, with x_1 the polarization direction and x_3 the propagation direction. The equations of motion for a perfectly resonant particle can be integrated most conveniently in the case $x_2 = 0$, so that the axial magnetic field vanishes. As shown below, this is the most interesting case for high-energy photoelectron production. In matrix form, the equations of motion are $dx/ds = cu$ and $du/ds = \Omega u$, where $x(s)$ is the world line of the particle, $u(s)$ is the four-velocity, and $\Omega(s) = a(s)\omega F(s)$. The parameter s is the proper time, $a(s) = qE(s)/mc\omega$, E is the electric field, q is the charge of the particle, m is the mass, and ω is the frequency of the radiation. Using the coordinate system described above, the matrix F is

$$F(s) = \begin{pmatrix} 0 & 1 & 0 & \epsilon(s) \\ 1 & 0 & 0 & -1 \\ 0 & 0 & 0 & 0 \\ \epsilon(s) & 1 & 0 & 0 \end{pmatrix}. \tag{1}$$

Here, ϵ is the ratio of axial-to-transverse electric field, which need not be small. Define a phase resonant particle as one for which Ω slowly varies on $x(s)$. Such particles have $x(s)$ confined to the intersection of two regions, one being a neighborhood about a hypersurface of constant ϵ and the other a neighborhood about a hypersurface of constant phase. In the first approximation, Ω is constant, and the solution of the velocity equation is $u(s) = \Lambda(s)u(0)$, where

$$\Lambda(s) = e^{\Omega(s)s}. \tag{2}$$

It can be shown that Λ is a Lorentz transformation, i.e., $\Lambda^T g \Lambda = g$, where T indicates the transpose, and $g = \mathrm{diag}(1, -1, -1, -1)$. Of particular interest is the initial condition $u(0) = (1,0,0,0)^T$, which, according to most theories, holds for an electron at the moment of ionization, at least when the atomic number satisfies $Z \ll 137$. In this case,

$$u(s) = \frac{1}{\epsilon^2} \begin{pmatrix} \cosh\epsilon\sigma - 1 + \epsilon^2 \cosh\epsilon\sigma \\ \epsilon - \epsilon\cosh\epsilon\sigma + \epsilon\sinh\epsilon\sigma \\ 0 \\ \cosh\epsilon\sigma - 1 + \epsilon^2\sinh\epsilon\sigma \end{pmatrix}, \tag{3}$$

where $\sigma(s) = a_0\omega s$. In the plane-wave limit ($\epsilon \to 0$) the particle momentum is

$$u(s) = \begin{pmatrix} 1 + \sigma^2/2 \\ \sigma \\ 0 \\ \sigma^2/2 \end{pmatrix}. \tag{4}$$

As expected, taking the plane-wave limit leads to the invariance of [8,9]

$$\Upsilon \equiv u_0 - u_3. \tag{5}$$

Moreover, when $\sigma \gg 1$, the momentum is predominantly in the forward direction, i.e., $u_3 \gg u_1$. Assuming $a_0 \gg 1$, this requires that ωs be at least of order unity; i.e., the time elapsed according to a clock moving with the particle should read at least one laser period, as measured by a laboratory frame clock. This does not necessarily violate the assumption that the particle should stay in phase, since the two clocks may keep very different time.

In order to estimate the maximum energy gain, values for s and ϵ are needed. The value of s is constrained by either phase slippage or interaction length. The phase change after a proper time s is

$$\varphi(s) = \int \omega(u_0 - u_3)ds = \frac{1 - \cosh\epsilon\sigma + \sinh\epsilon\sigma}{\epsilon a_0}, \tag{6}$$

whereas the distance traversed by the particle is

$$\begin{aligned} x_3(s) &= c\int u_3(s)ds \\ &= \frac{\lambda}{2\pi\epsilon^3 a_0}[\sinh\epsilon\sigma - \epsilon\sigma + \epsilon^2(\cosh\epsilon\sigma - 1)], \end{aligned} \tag{7}$$

where $\lambda = 2\pi c/\omega$. The maximum energy gain is $u_0(s')$, where $s' = \min\{s|\varphi(s) = \pi/4, s|x_3(s) = z_R\}$. Here, $z_R = \pi r_0^2/\lambda$ is the Rayleigh length, with r_0 the radius of the beam waist. A characteristic value for ϵ is obtained by evaluating the field at the point $(r_0,0,z_R)$, which gives $\epsilon^2 = \lambda/4\pi z_R$. The phase resonance limit corresponds to the case where the energy gain is limited by the interaction length, i.e., the case where $x_3(s') = z_R$.

Closed expressions for $u_0(s')$ can be obtained by expanding s' to some desired order in ϵ. More generally, s' can be found numerically. The zero-order analytical solution, in the phase resonance limit, is

$$u_{0,\max}^{(0)} = 1 + 2\left(\frac{3\pi r_0}{\lambda}\right)^{2/3}\left(\frac{P r_e}{mc^3}\right)^{1/3}, \tag{8}$$

where P is the laser power and r_e is the classical electron radius. As an example, a 10-PW laser pulse, with $\lambda = 0.8$ μm, focused to $r_0 = 5$ μm, gives $a_0 \approx 100$, and $u_{0,\max}mc^2 \approx 1.5$ GeV. The phase resonance curve in Fig. 1 uses the numerical solution for s', which leads to closer agreement with simulation. Note that in the first approximation, the wavelength appears only in the combination r_0/λ, which is fixed by the focusing geometry.

An expression for the phase resonance threshold amplitude is obtained by equating the ponderomotive energy with the lowest order phase resonance energy and solving for a_0 (i.e., the threshold is estimated as the point where the two curves intersect). This results in

$$a_0^{\text{thresh}} = 2^{7/4}\sqrt{3}\frac{\pi r_0}{\lambda} \approx \frac{6\pi r_0}{\lambda}. \tag{9}$$

It should be noted that the whole of the foregoing theory assumes paraxial focusing, i.e., $r_0 \gg \lambda$. As a result, it is evident that a_0 must always be large.

The essential element in the foregoing analysis is the assumption that upon ionization into an extreme field, an electron can be accelerated to nearly the speed of light in a fraction of an optical cycle. This requires that the ionization potential be large enough so that the electron is held in position by its parent ion until it is exposed to ultrarelativisitic intensity, but not so large that ionization becomes highly improbable.

IV. PHOTOELECTRON DISTRIBUTIONS

In order to calculate detailed photoelectron distributions numerically, a large number of trials of the two-step model are carried out, using a paraxial model for the vector fields in a laser focus and an advanced, covariant, particle tracking model [12]. Tracking photoelectrons through this field gives the quasiclassical S matrix, S_{xu}, where $|S_{xu}|^2$ is the probability that a photoelectron with initial coordinate x has final momentum u. Here, x_0 is the time of ionization, while $\mathbf{x} = (x_1,x_2,x_3)$ is the position of the parent ion. The parameter x_0 falls out of the two-step ionization model and is only defined quasiclassically. The dependence on $\mathbf{x}$ is present in the quantum mechanical S matrix but is often ignored because it disappears in the plane-wave limit.

Consider laser parameters $a_0 = 100$, $\lambda = 0.8$ μm, $r_0 = 5$ μm, and $\tau = 30$ fs, which are chosen to be achievable by near-term 10-PW laser systems. Projections of the quasiclassical S matrix for Ar^{17+}, correlating the final energy with the initial coordinate, are shown in Fig. 2. In any given projection, there is a large low-energy population and only a small number of high-energy particles. The highest energy particles originate roughly from the coordinates $x_1 \approx \pm r_0$, $x_2 \approx 0$, and $x_3 \approx 0$. This suggests that a high-quality, high-energy beam might be obtained by localizing the parent ions to a small neighborhood about one or both of these two points.

The photoelectron distribution from a single Ar^{17+} ion, for two different ion coordinates, is shown in Fig. 3. This is computed using 10^6 trials of the two-step model, with the ion coordinate $\mathbf{x} = 0$ in Fig. 3(a) and the ion coordinate $\mathbf{x} = (r_0,0,z_R)$ in Fig. 3(b). The case with the ion at the origin is nearly symmetric in u_1, with the slight asymmetry due to the fact that the first burst of ionization current must occur in a field with one sign or the other. The case with the ion offset from the axis is highly asymmetric in u_1, as might be expected. The departure from the parabolic form of the plane-wave case is obvious [4,21]. Interestingly, the fine structure exhibits a multiplicity of discrete contours. This structure can be understood in terms of the S matrix projected into the plane of the ionization phase, $\Phi_0 = \Phi(x_0,\mathbf{x})$, and energy [12]. For example, it is found that the densely packed low-energy contours in Fig. 3(b) are generated for $\Phi_0 \approx \pi/2 + 2\pi n$, where n is an integer, while the higher energy contours are generated for $\Phi_0 \approx 3\pi/2 + 2\pi n$. More importantly, each of the high-energy contours in the bundle of contours can be associated with a particular subcycle burst of ionization current, as shown in Fig. 3(c). This is intriguing because the temporal structure of the unobservable probability current is directly mapped to a corresponding observable structure.

V. CONCLUSIONS

Multipetawatt lasers access a new regime of strong-field physics and free-space acceleration, which appears when the

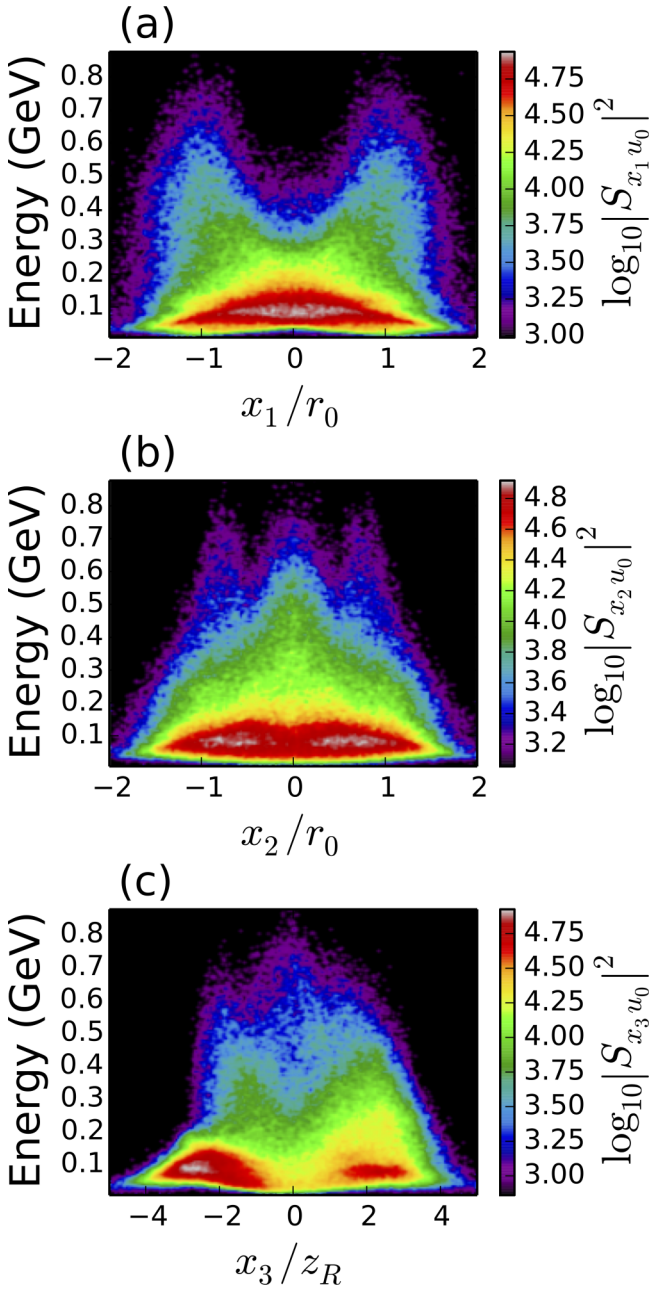

FIG. 2. Quasiclassical S-matrix projections for Ar^{17+}. Correlation of the final energy (a) with the initial polarization coordinate, (b) with the intial cross-polarization coordinate, and (c) with the initial axial coordinate. Variables not in the subscript of S are integrated out.

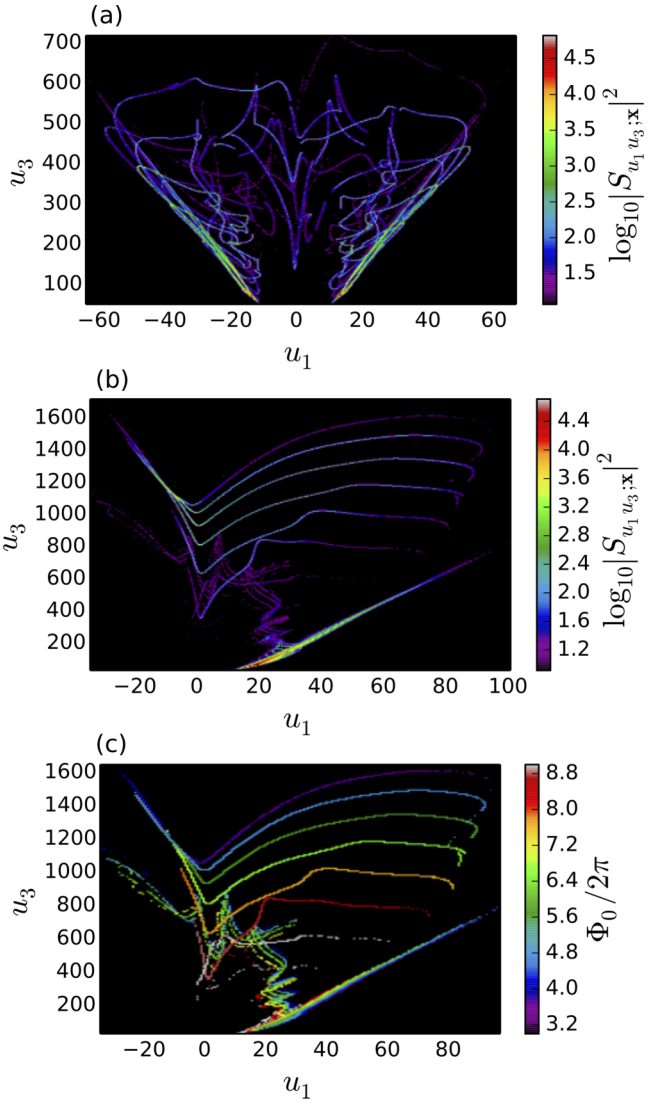

FIG. 3. Momentum distributions from an Ar^{17+} ion positioned (a) at $\mathbf{x}=0$ and (b) at $\mathbf{x}=(r_0,0,z_R)$. (c) Same as (b), except that the color scale identifies the average ionization phase associated with the given final momentum. The monochromaticity of a given contour illustrates that the entire contour is associated with a particular phase. Variables not in the subscript of S are integrated out.

normalized vector potential $a_0 \gtrsim 10$. When ionized electrons are released into an extreme field, they can be accelerated to superponderomotive energies due to phase resonance; i.e., they stay near the same optical phase throughout a substantial portion of the confocal region. The resulting photoelectron momentum distributions have unique features, which depart significantly from the usual parabolic form expected in the plane-wave or weakly relativistic limits. Single atoms, or possibly clusters of atoms, produce discrete contours in momentum space that can be related to subcycle bursts of ionization current. The narrow, nonparabolic contours in momentum space suggest a potential application in the area of laser-plasma acceleration of electrons. Although superponderomotive tunneling ionization cannot compete with plasma as a primary accelerating structure, it may be useful as an injection source, i.e., as the front end of a laser-plasma accelerator. This possibility was considered previously in Refs. [3] and [4] in the context of parabolic momentum-space contours. In particular, angular selection was proposed as a means of controlling the energy spread. The difficulty was the low charge resulting from the angular selection. The variety of nonparabolic momentum-space contours that occur in the superponderomotive regime raises further possibilities, which may allow for simultaneous extraction of high charge and low energy spread.

ACKNOWLEDGMENTS

We have enjoyed fruitful discussions affecting this work with many colleagues, including A. Ting, D. Kaganovich, M. H. Helle, R. F. Hubbard, L. Johnson, J. R. Peñano, J. Giuliani, J. Davis, A. Zigler, A. S. Landsman, A. Noble, K. Krushelnick, A. Maksimchuk, E. Chowdhury, D. Schumacher, and E. Turcu. This work was supported by the Naval Research Laboratory 6.1 Base Program.

[1] I. Turcu *et al.*, Roman. Rep. Phys. **68**, S144 (2016).
[2] D. Gordon, B. Hafizi, and M. Helle, J. Comput. Phys. **267**, 50 (2014).
[3] C. I. Moore, A. Ting, S. J. McNaught, J. Qiu, H. R. Burris, and P. Sprangle, Phys. Rev. Lett. **82**, 1688 (1999).
[4] C. I. Moore, A. Ting, T. Jones, E. Briscoe, B. Hafizi, R. F. Hubbard, and P. Sprangle, Phys. Plasmas **8**, 2481 (2001).
[5] B. Pollock, C. Clayton, J. Ralph, F. Albert, A. Davidson, L. Divol, C. Filip, S. Glenzer, K. Herpoldt, W. Lu *et al.*, Phys. Rev. Lett. **107**, 045001 (2011).
[6] B. Hidding, G. Pretzler, J. B. Rosenzweig, T. Konigstein, D. Schiller, and D. L. Bruhwiler, Phys. Rev. Lett. **108**, 035001 (2012).
[7] H. Reiss, Prog. Quantum Electron. **16**, 1 (1992).
[8] V. Popov, Phys. Usp. **47**, 855 (2004).
[9] M. Klaiber, E. Yakaboylu, and K. Z. Hatsagortsyan, Phys. Rev. A **87**, 023418 (2013).
[10] B. Hafizi, D. Gordon, and J. Palastro, Phys. Rev. Lett. (to be published) (2017).
[11] P. B. Corkum, N. H. Burnett, and F. Brunel, Phys. Rev. Lett. **62**, 1259 (1989).
[12] See Supplemental Material at http://link.aps.org/supplemental/10.1103/PhysRevA.95.033403 for details.
[13] L. V. Keldysh, Sov. Phys. JETP **20**, 1307 (1965).
[14] G. L. Yudin and M. Y. Ivanov, Phys. Rev. A **64**, 013409 (2001).
[15] L. Landau and E. Lifschitz, *Physical Kinetics* (Pergamon Press, Oxford, UK, 1980).
[16] S. X. Hu and A. F. Starace, Phys. Rev. Lett. **88**, 245003 (2002).
[17] L.-W. Pi, S. X. Hu, and A. F. Starace, Phys. Plasmas **22**, 093111 (2015).
[18] S. S. Luo, P. D. Grugan, and B. C. Walker, Phys. Rev. A **91**, 033412 (2015).
[19] A. DiChiara, I. Ghebregziabher, J. Waesche, T. Stanev, N. Ekanayake, L. Barclay, S. Wells, A. Watts, M. Videtto, C. Mancuso *et al.*, Phys. Rev. A **81**, 043417 (2010).
[20] P. Mora and T. M. Antonsen, Phys. Plasmas **4**, 217 (1997).
[21] B. Hafizi, P. Sprangle, J. R. Peñano, and D. F. Gordon, Phys. Rev. E **67**, 56407 (2003).